

We are IntechOpen, the world's leading publisher of Open Access books Built by scientists, for scientists

4,800

Open access books available

122,000

International authors and editors

135M

Downloads

Our authors are among the

154

Countries delivered to

TOP 1%

most cited scientists

12.2%

Contributors from top 500 universities



WEB OF SCIENCE™

Selection of our books indexed in the Book Citation Index
in Web of Science™ Core Collection (BKCI)

Interested in publishing with us?
Contact book.department@intechopen.com

Numbers displayed above are based on latest data collected.
For more information visit www.intechopen.com



High Performance Metasurface Antennas

Haisheng Hou, Haipeng Li, Guangming Wang, Tong Cai, Xiangjun Gao and Wenlong Guo

Abstract

Recently, metasurfaces (MSs) have received tremendous attention because their electromagnetic properties can be controlled at will. Generally, metasurface with hyperbolic phase distributions, namely, focusing metasurface, can be used to design high-gain antennas. Besides, metasurface has the ability of controlling the polarization state of electromagnetic wave. In this chapter, we first propose a new ultrathin broadband reflected MS and take it into application for high-gain planar antenna. Then, we propose multilayer multifunctional transmitted MSs to simultaneously enhance the gain and transform the linear polarization to circular polarization of the patch antenna. This kind of high-gain antenna eliminates the feed-block effect of the reflected ones.

Keywords: focusing, metasurface, high-gain, polarization conversion, reflection, transmission

1. Single-layer broadband planar antenna using ultrathin high-efficiency focusing metasurfaces

Recently, metasurfaces (MSs) have attracted growing interests of many researchers due to their planar profile, easy fabrication, and also strong beam control capacity [1–6]. For phase gradient metasurfaces (PGMS), proposed by Yu et al. [7], a wide range of applications have been found, such as anomalous beam bending [8, 9], focusing [7, 10], surface-plasmon-polariton coupling [11, 12], and polarization manipulation. With the ability of tuning the phase range covering 2π , metasurface can be used to improve performance of antenna. By fixing proper phase distributions on the metasurface, we can manipulate the wavefronts and the polarizations of the electromagnetic waves (EM) at will.

The focusing metasurface, which is one kind of functional metasurfaces, can focus the incident plane wave to its focal point. These characters indicate that the focusing metasurface can be applied for designing planar high-gain antenna by placing the feed sources at the focal point over the focusing metasurface [1]. Generally, there are two types of focusing metasurface, namely, reflective focusing metasurface and transmitted focusing metasurface. Based on upon two types of focusing metasurface, there are two kinds of high-gain antenna, namely, reflective metasurface high-gain antenna and transmissive metasurface high-gain antenna. Compared with the reflective metasurface antenna based on the focusing metasurface, transmissive metasurface antenna avoids the feed blockage effect,

making it more suitable for a high-gain antenna design. Besides, when designing a reflective focusing metasurface, the reflection magnitude is close to 1 (0 dB) due to grounded plane composed of PEC. Therefore, the reflection phase is the only modulated character by the focusing metasurface. However, transmitted phase and amplitude are both needed to be considered when designing a transmissive focusing metasurface. In [1], a dual-mode and dual-band flat high-gain antenna based on focusing metasurface is proposed. The reflection beam and transmission beam can be obtained. In [2], the modified I-shaped particles, which can independently manipulate the phases and amplitudes of the cross-polarization waves, have been proposed. Based on the proposed unit cell, three high-gain antennas are fabricated and tested. In [5], a novel split beam antenna using transmission-type coding metasurface is proposed, which provides a new way to design focusing metasurface. Although reflective metasurface antenna and transmissive metasurface antenna have been studied for many years, more efforts should be done to improve the performance (such as realized gain, bandwidth, polarization states, and so on) of antenna.

However, most reported metasurfaces suffer from a narrow bandwidth, which restrict their further applications, especially in planar antenna design. To overcome this drawback, several methods have been proposed such as using stacked phase shifting elements or aperture patches coupled to true-time delay lines. Besides, there is another way to obtain a broadband working width by using a single-layer broadband planar antenna using ultrathin high-efficiency focusing metasurfaces.

In this chapter, a single-layer broadband focusing metasurface has been proposed to enhance the gain of the antenna. Theoretically, the spherical wave emitted by a point source at the focal point can be transformed to a plane wave. Therefore, a Vivaldi antenna has been fixed at the focal point of focusing metasurface, obtaining wideband planar antennas. In this case, the directivity and gain of the point source have been improved remarkably.

1.1 Element design

Figure 1 shows the proposed element, which is used to design reflective metasurface. The element is composed of orthogonally I-shaped structures and a metal-grounded plane spaced by a dielectric isolator with a permittivity of

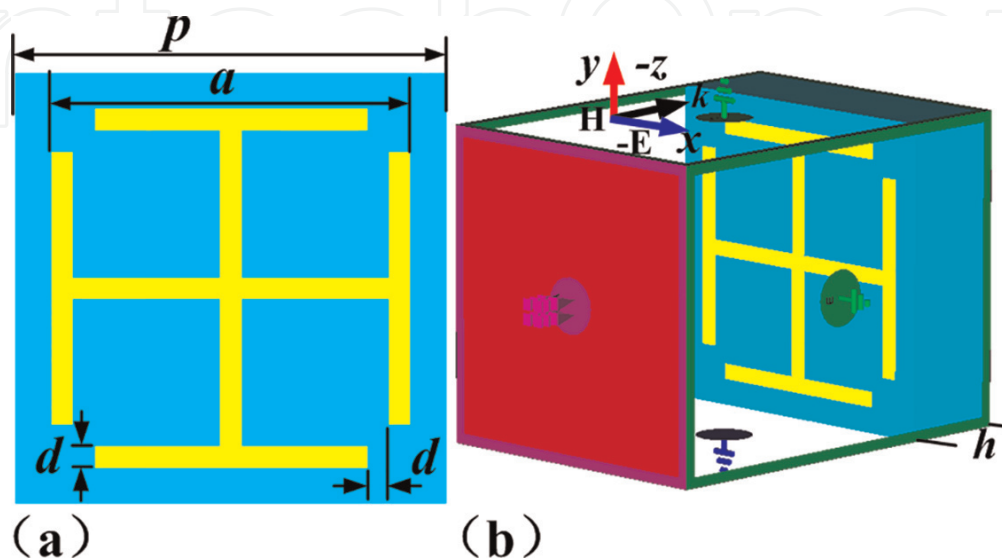


Figure 1. Structure of the element and the simulated setup: (a) top view; (b) perspective view. The parameters are listed as $d = 0.3 \text{ mm}$, $p = 6 \text{ mm}$, $h = 2 \text{ mm}$, and $a = 1.8\text{--}5 \text{ mm}$.

$\epsilon_r = 2.65$, loss tangent of 0.001, and thickness of 2 mm. For characterization, the element is simulated in commercial software CST Microwave Studio, unit cell boundary conditions are employed along x and y directions. Moreover, the element is illuminated by x -polarized plane wave along $-z$ direction.

Figure 2 shows the reflective phase of the reflection wave versus the length of parameter a . To demonstrate the ability of tuning the reflective phase at broadband, the reflective phases versus parameter a varying from 1.8 to 5 mm have been plotted from 15 to 22 GHz in **Figure 2**, respectively. Obviously, the phase tuning range is covering 2π at all frequencies (15–22 GHz). In additions, the eight phase shift curves nearly parallel to each other, leading to a large bandwidth for focusing EM wavefronts.

1.2 Broadband and focusing metasurface design

Generally, the reflected wave will always deflect to the phase delay direction according to the general reflection law as depicted in Eq. (1):

$$n_r \sin(\theta_r) - n_i \sin(\theta_i) = \frac{\lambda}{2\pi} \frac{d\Phi}{dx} \quad (1)$$

where Φ is the phase discontinuity at the local position on the metasurface, θ_r/θ_i is the reflected/incident angle, n_r/n_i is the reflective index of the reflected/incident medium, and λ is the wavelength. To clearly demonstrate the general reflection law, $d\Phi/dx$ can be denoted as $2\pi/np$, where n is the number of elements arranged in order along x direction and p is the periodicity of element. In such case, the element is illuminated normally, so the θ_i can be denoted by 0° . At the same time, the $n_i = 1$ can be realized because the element is placed in free space. Consequently, the reflected angle θ_r can be depicted in Eq. (2):

$$\theta_r = \sin^{-1}\left(\frac{\lambda}{2\pi} \times \frac{2\pi}{np}\right) \quad (2)$$

Then designing a focusing phase distribution on the metasurface by using the proposed element is the key procedure. Based on Fermat's principle, the EM

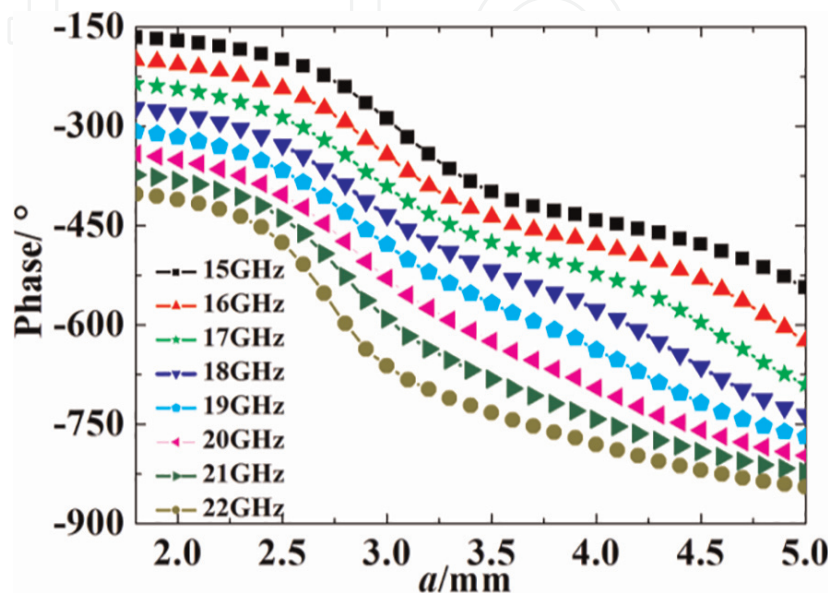


Figure 2.
 Reflected phase shift with a (1.8–5 mm) from 15 to 22 GHz.

wavefront can be modified by changing the phase distribution on the metasurface. In order to focus the incident plane wave to a quasi-spherical wave, the phase $\Phi(m,n)$ imposed at location (m,n) should satisfy Eq. (3):

$$\Phi(m,n) = \frac{2\pi}{\lambda} \left(\sqrt{(mp)^2 + (np)^2 + L^2} - L \right) + \Phi_0 \quad (3)$$

where L is the focal length, Φ_0 is the phase of origin point $(0,0)$, and p is the periodicity of the element. **Figure 3a** depicts the conversion of an incident plane wave to a quasi-sphere wave, and **Figure 3b** depicts the conversion of a quasi-sphere wave to plane wave using the focusing metasurfaces.

Based on the procedure, a focusing metasurface with a size of $90 \times 90 \text{ mm}^2$, composed of 15×15 elements, is proposed and simulated. By theoretically calculating, a hyperbolic phase distribution is assigned on the metasurface. As shown in **Figure 4a** shows, the phase response along x direction is a hyperbolic phase distribution, and **Figure 4b** is a plot of the whole phase distribution on the metasurface.

In order to have an intuitionistic view of the focusing metasurface, the proposed metasurface, as shown in **Figure 5a**, is simulated in the commercial software CST.

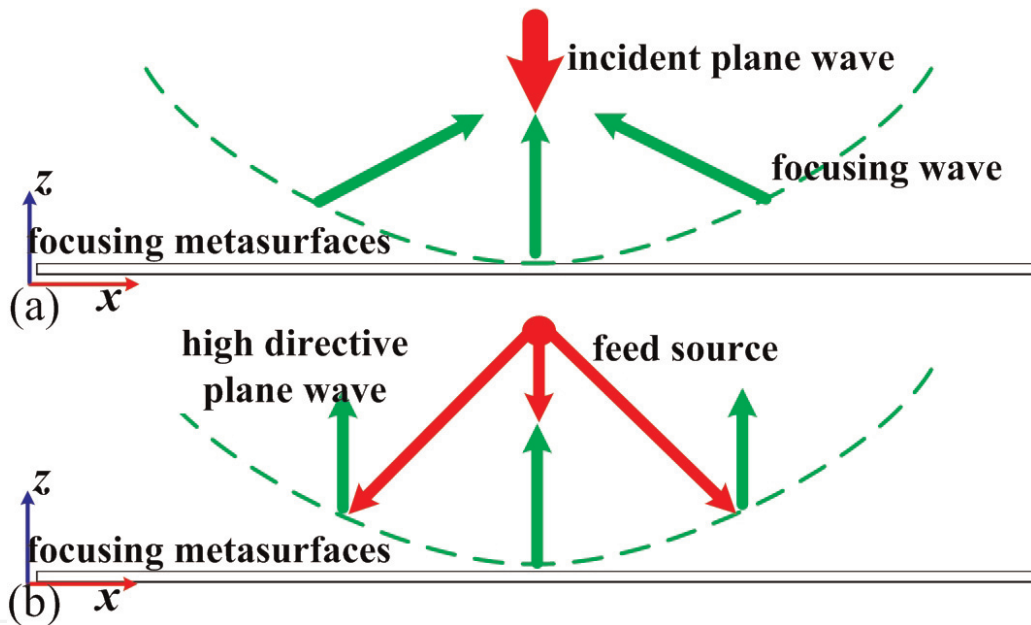


Figure 3. (a) Schematic used to describe focusing effect and (b) schematic used to describe operating mechanism of planar antenna.

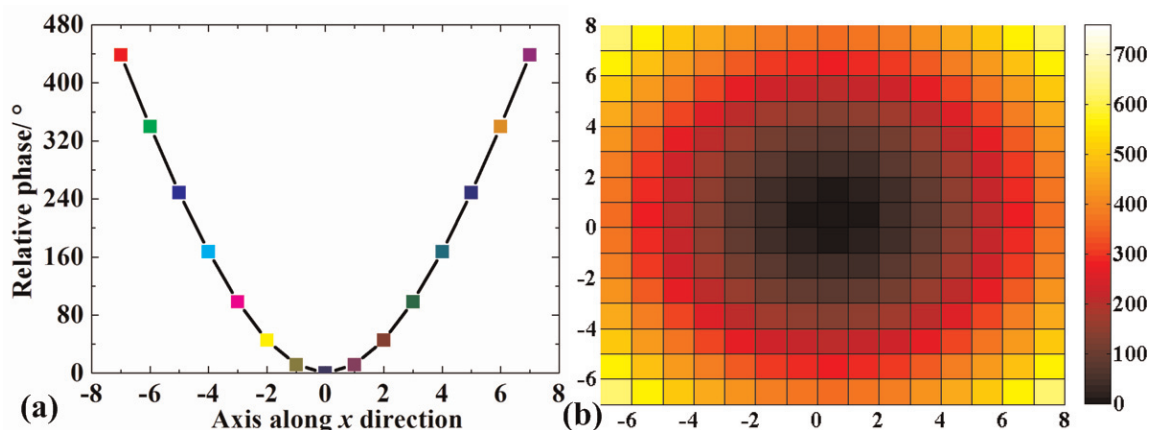


Figure 4. (a) Phase response on the cut line along x direction and (b) relative reflection phase distribution in xoy plane.

The metasurface is illuminated by a plane wave with a polarization propagating along $-z$ direction. To verify the focusing effect, the electrical field at both yoz and xoz planes in the center frequency 18 GHz is plotted in **Figure 5b** and **c**. It is obvious that the incident plane wave is transformed into quasi-sphere wave in the orthogonal planes. Furthermore, to verify the position of the focus point, a curve is put along z direction, and power field is evaluated on the curve. As **Figure 5d** shown, the energy is focused at both xoz and yoz planes. The red spot is the focus point. Normalized power field versus the distance to the metasurface is described in **Figure 5d**. Observing the normalized power field, it is drawn that the focal point is at $L = 33$ mm, which agrees well with the theoretical calculation.

1.3 Broadband and high-gain planar antenna design

According to the above analysis, a spherical wave, emitted by a source located at focal point of the focusing metasurface, can be transformed into a plane wave theoretically. Therefore, a high-gain planar antenna can be realized by putting a feed antenna at the focal point of the focusing metasurface. The well-designed feed antenna is a Vivaldi antenna to offer a wide operating bandwidth. **Figure 6a** depicts

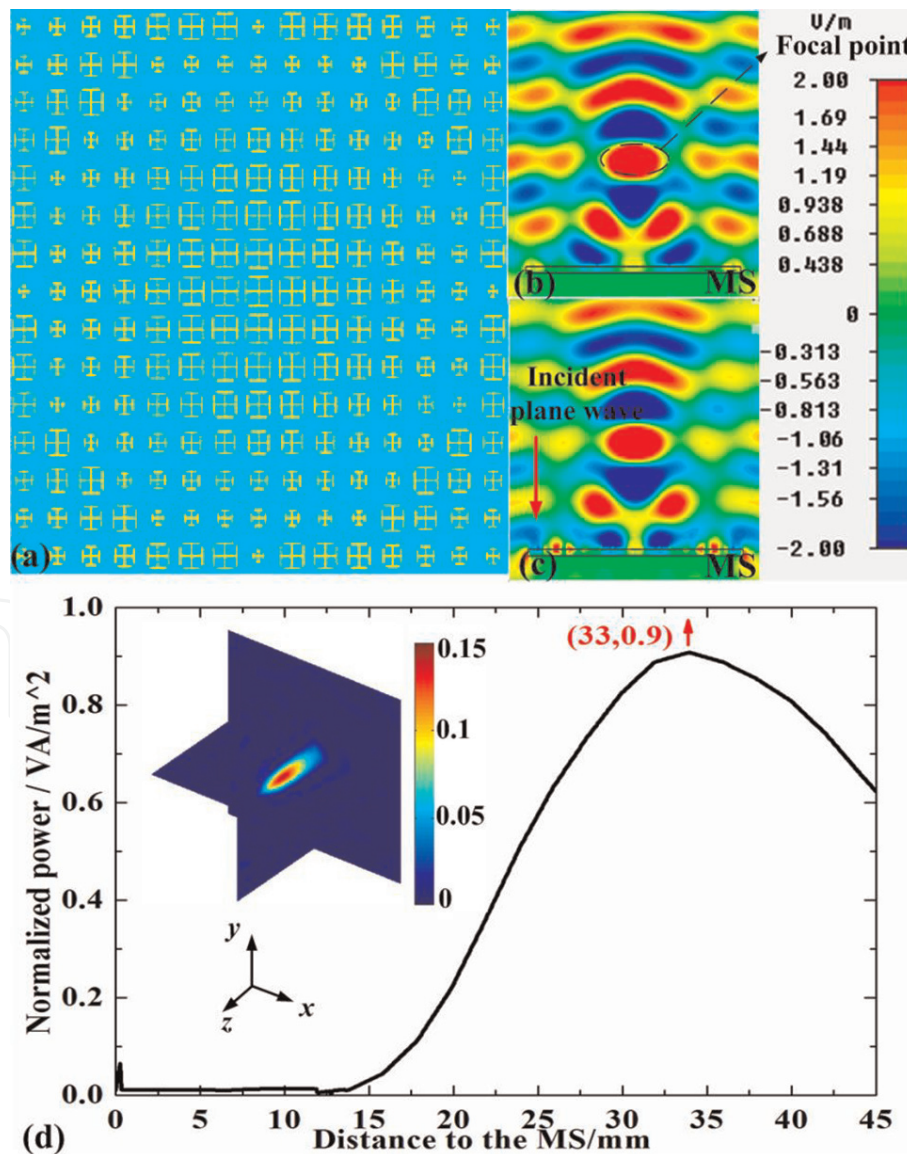


Figure 5. (a) The simulated focusing MS; (b) simulated reflected electric field distribution in yoz plane at 18 GHz; (c) simulated reflected electric field distribution in xoz plane at 18 GHz; and (d) power distribution of focusing wave at 18 GHz and distance to the MS.

the geometry parameters of Vivaldi antenna, and **Figure 6b** plots the reflection coefficient. It is clear to find that the designed antenna can operate from 15 to 22 GHz with the S_{11} lower than -10 dB, indicating that the proposed feed antenna is a good feed source for the planar antenna.

To demonstrate the performance of the planar antenna, the simulated electrical field distributions with/without focusing metasurface at both xoz and yoz planes are

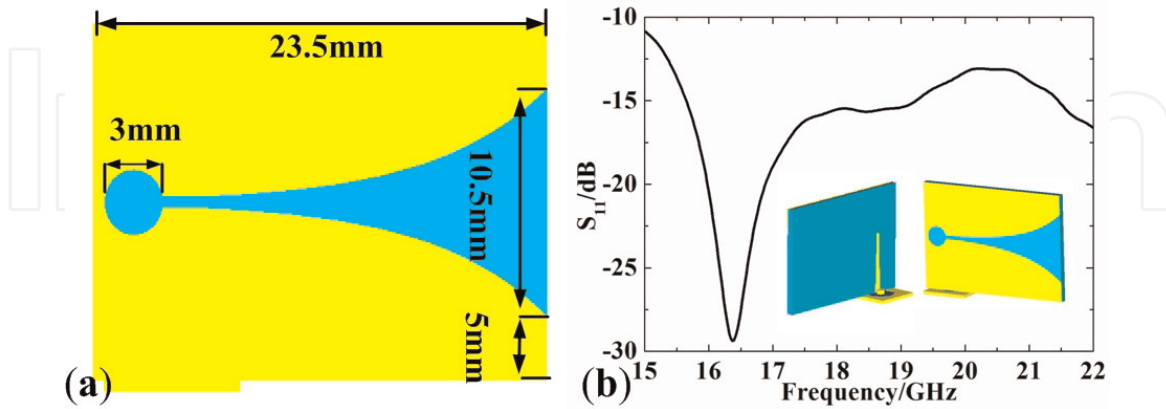


Figure 6. (a) Parameters of Vivaldi antenna and (b) simulated S_{11} of Vivaldi antenna.

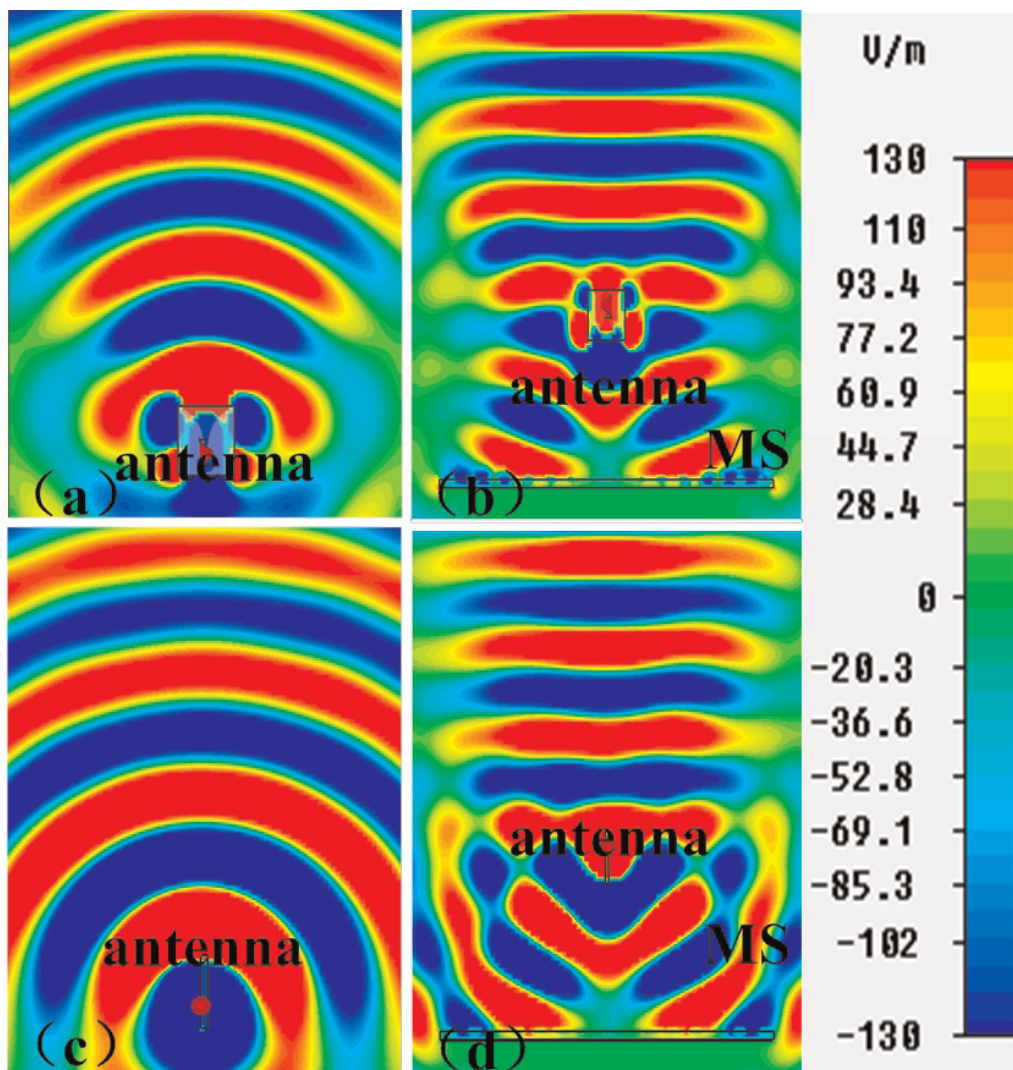


Figure 7. Simulated electric field distribution at 15 GHz in (a and b) yoz plane and (c and d) xoz plane, respectively, for the Vivaldi antenna without (a and c) and (b and d) with the PGMS.

simulated. **Figures 7–9** plot the electrical field distributions at three representative frequencies (15, 18, and 22 GHz). As expected, the spherical wave emitted by feed antenna is transformed into nearly plane wave with the focusing metasurface in both xoz and yoz plane.

To clearly show the farfield performance of the planar antenna, the 3D radiation patterns at 15, 18, and 22 GHz are shown in **Figure 10**. The gain has been remarkably enhanced in a broad bandwidth comparing with the gain of the feed antenna. And pencil-shaped radiation pattern is achieved. Thus, the broadband and high-gain planar antenna is obtained. In order to verify the simulation, a sample composed of 15×15 elements is fabricated as **Figure 11a** shown. Besides, the designed Vivaldi antenna is fabricated and put at the focal point with a foam.

The simulated and measured radiation patterns in xoz plane and yoz plane at 18 GHz are plotted in **Figure 12**. It is obvious that the designed planar antenna has a remarkably enhanced gain compared to without focusing metasurface. The peak gain enhancement is about 15 dB relative to the bare Vivaldi antenna both in xoz plane and yoz plane. To demonstrate the broadband performance of the high-gain planar antenna, the simulated and measured gain versus frequency is described in **Figure 13**. It can be concluded that 3-dB gain bandwidth is from 15 to 22 GHz and the measured results conform to simulation well. Due to thin thickness, polarization

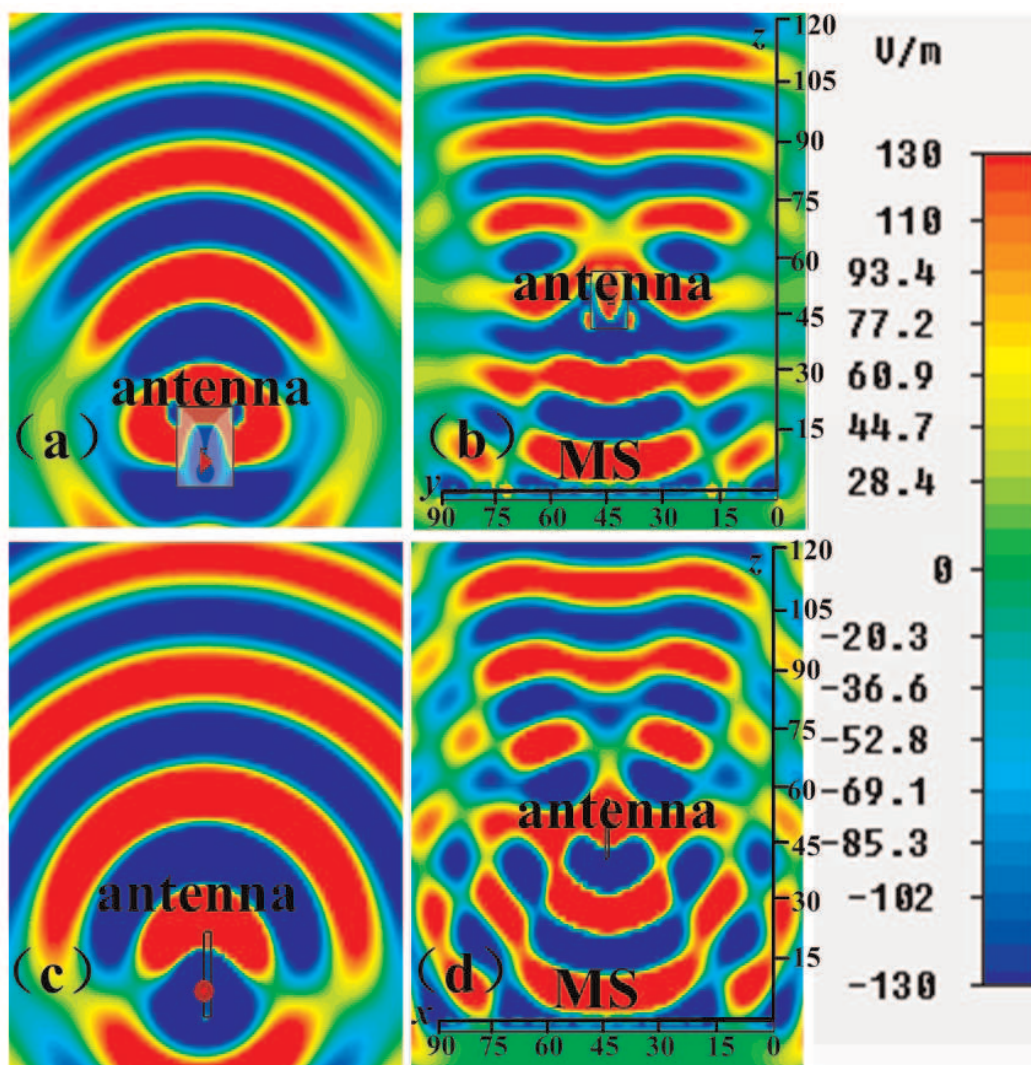


Figure 8. Simulated electric field distribution at 18 GHz in (a and b) yoz plane and (c and d) xoz plane, respectively, for the Vivaldi antenna without (a and c) and (b and d) with the PGMS.

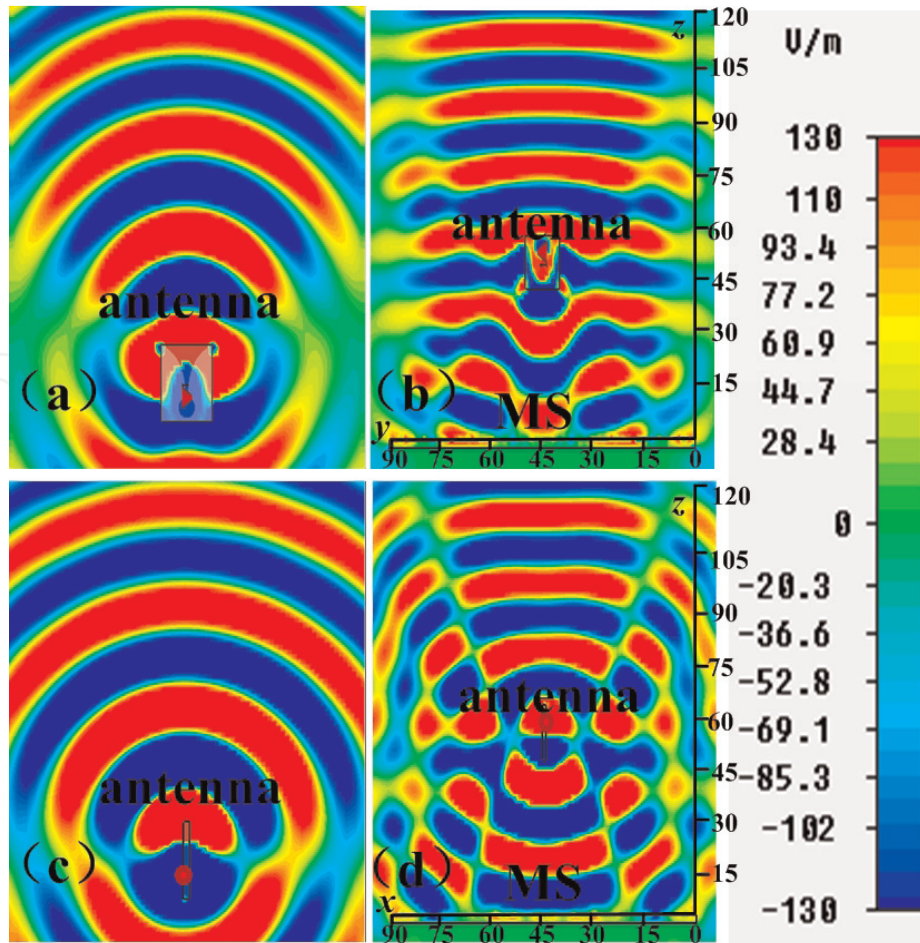


Figure 9. Simulated electric field distribution at 22 GHz in (a and b) yoz plane and (c and d) xoz plane, respectively, for the Vivaldi antenna without (a and c) and (b and d) with the PGMS.

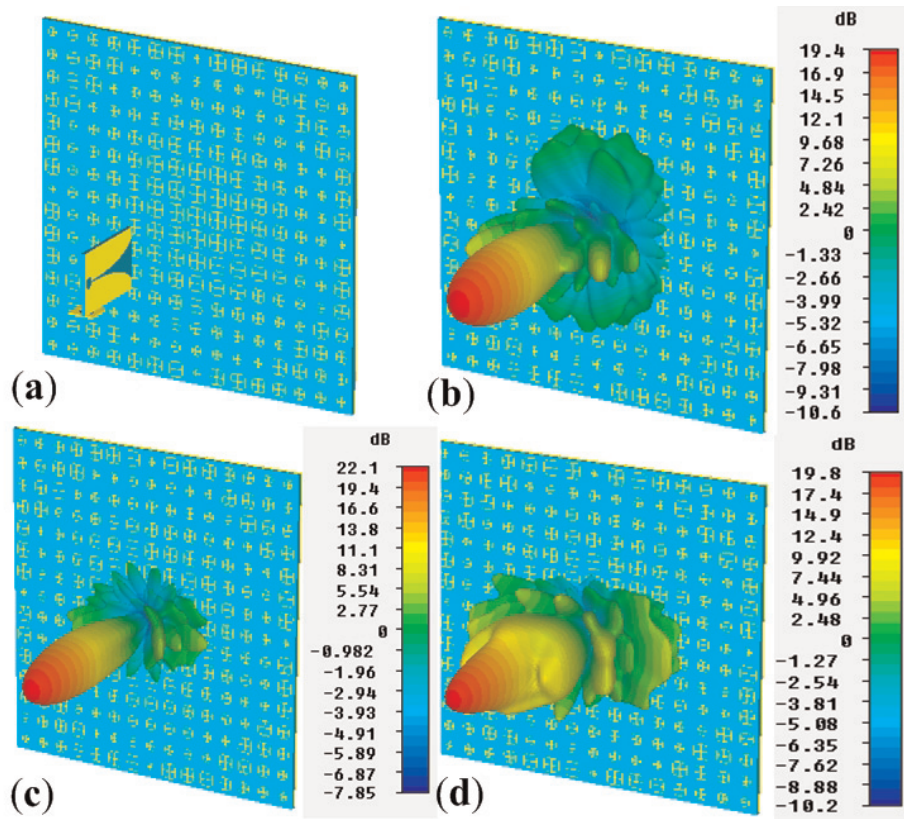


Figure 10. (a) Simulated model for planar antenna and 3D radiation pattern for (b) 15 GHz; (c) 18 GHz; and (d) 22 GHz.

insensitivity, and broad bandwidth, the proposed broadband high-gain planar antenna opens up a new route for the applications of the metasurface in microwave band.

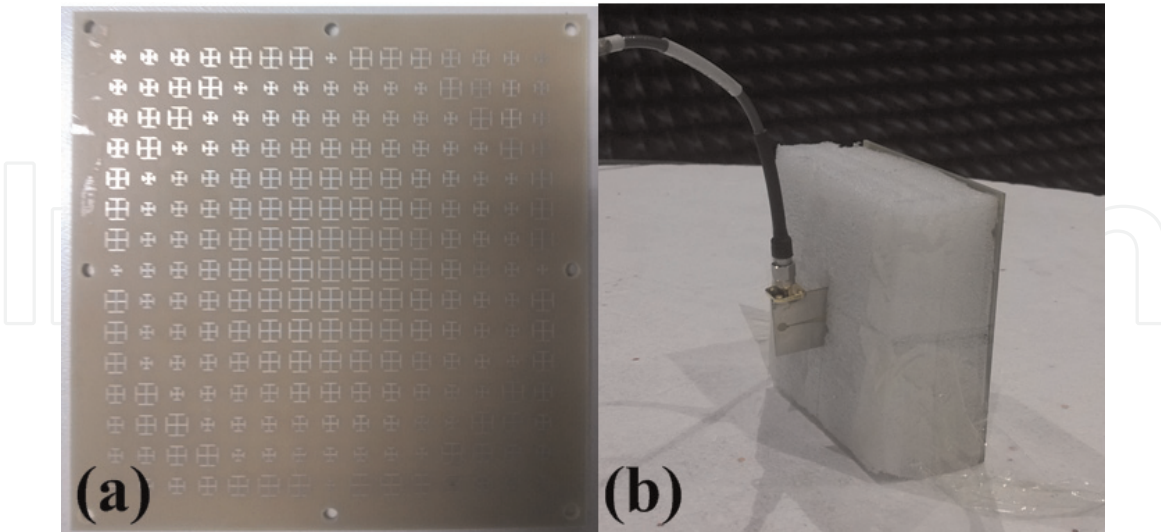


Figure 11. The photographs of (a) metasurfaces top view and (b) planar high-gain antenna.

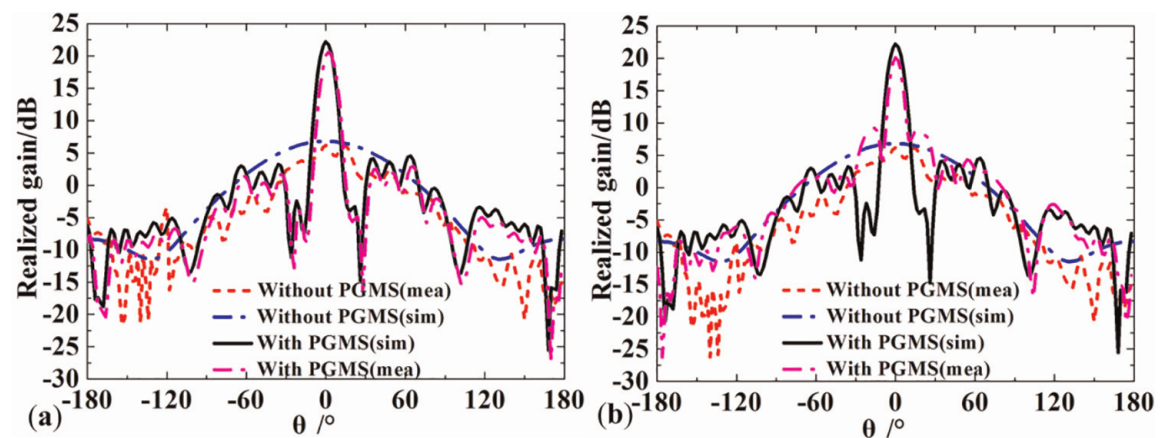


Figure 12. Simulated and measured farfield radiation pattern at 18 GHz (a) xoz plane and (b) yoz plane.

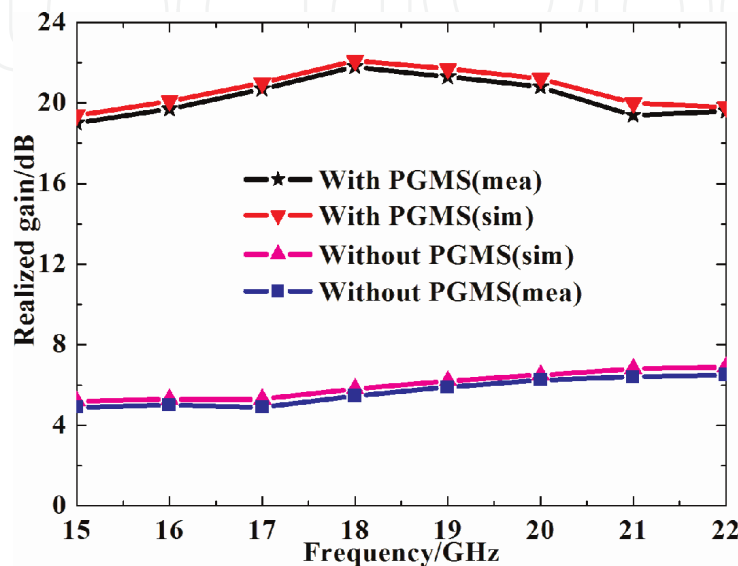


Figure 13. Simulated and measured realized gain with/without PGMS from 15 to 22 GHz.

2. Highly efficient multifunctional metasurface for high-gain lens antenna application

With the development of the metasurface, it is a trend to design multifunctional devices to satisfy increasing requests of communication system in microwave region. Due to the ability of solving some key challenges like susceptibility to multipath, atmospheric absorptions, and reflections, circularly polarized antennas play an important role in wireless and satellite communication. At the same time, high-gain antenna plays an essential role in achieving long-distance wireless communication.

Owing to the function of linear-to-circular polarization conversion [13–17], metasurface opens up a novel route to realize the circular polarization. Therefore, it is interesting to design a circular antenna with high gain using metasurface. Generally, there are two categories of metasurface—transmitting type and reflecting type—according to the format of the metasurface. Compared with reflecting type, transmitting type allows reducing feed blockage effect when designing high-gain antenna. Therefore, it is more suitable for high-gain antenna. And it will be more novel to design a circularly polarized high-gain antenna engineered to realize linear-to-circular polarization conversion and EM waves focusing by transmitting metasurface.

2.1 Theoretical analysis of transmitted linear-to-circular polarization conversion

Assuming that the EM wave propagates through an arbitrary transmitted metasurface placed on xoz plane ($z = 0$), for simplicity, we only consider normal incidence illumination. Therefore, it can be assumed that an incident wave propagates along $-z$ direction. Then the incident wave's electric field can be described as

$$\vec{E}_i = (\hat{x}E_x + \hat{y}E_y) \quad (4)$$

$$\begin{pmatrix} E_x \\ E_y \end{pmatrix} = \begin{pmatrix} \cos \theta \\ \sin \theta \end{pmatrix} e^{-jkz} \quad (5)$$

where k is the wave number, θ is the angle along x axis, and complexes E_x and E_y represent the x -polarized and y -polarized states, respectively. The transmitted electric field through the metasurface can be described as [18]

$$\vec{E}_t = (\hat{x}E'_x + \hat{y}E'_y) \quad (6)$$

$$\begin{pmatrix} E'_x \\ E'_y \end{pmatrix} = T \begin{pmatrix} E_x \\ E_y \end{pmatrix} \quad (7)$$

Furthermore, the complex amplitudes of the incident and transmitted fields can be connected by the T matrix (transmission matrix) [19]:

$$T = \begin{pmatrix} T_{xx} & T_{xy} \\ T_{yx} & T_{yy} \end{pmatrix} \quad (8)$$

where T_{ij} represents the transmission coefficient of j -polarized incident wave and i -polarized transmission wave. Thus, the incident wave of linear polarization

can be transformed to transmitted wave of a right-handed circular polarized (RHCP) or a left-handed circular polarized (LHCP).

As depicted in **Figure 14**, there are two typical cases of realizing linear-to-circular polarized conversion.

Take the case of $\theta = 45^\circ$ as an example; the metasurface is illuminated with a linear polarization incident wave with the incident electric field E , titled 45° relative to $+x$ direction. Thus the vertical and horizontal components of E are set as

$$\begin{pmatrix} E_x \\ E_y \end{pmatrix} = \frac{1}{\sqrt{2}} \begin{pmatrix} 1 \\ 1 \end{pmatrix} e^{-jkz} \quad (9)$$

Therefore, the vertical and horizontal components of the transmitted electric field E can be denoted as

$$\begin{pmatrix} E'_x \\ E'_y \end{pmatrix} = T \frac{1}{\sqrt{2}} \begin{pmatrix} 1 \\ 1 \end{pmatrix} e^{-jkz} \quad (10)$$

To get the circular polarization, the amplitudes of E for vertical and horizontal components are ideally equal, and the phase of E for vertical and horizontal components experiences the distinct 90° phase shift, namely, $\text{Mag}(E'_x) = \text{Mag}(E'_y)$ and $\text{Arg}(E'_x) - \text{Arg}(E'_y) = -90^\circ$. Therefore, $\text{Mag}(T_{xx}) = \text{Mag}(T_{yy}) = 1$, $\text{Mag}(T_{xy}) = \text{Mag}(T_{yx}) = 0$, and $\text{Arg}(T_{xx}) - \text{Arg}(T_{yy}) = -90^\circ$ should be satisfied. At the same time, $\text{Arg}(T_{ij})$ represents the phase of j -polarized incident wave into i -polarized transmission wave. And $\text{Mag}(T_{ij})$ represents the amplitude of j -polarized incident wave into i -polarized transmission wave. In this case, the T matrix is

$$T = \begin{pmatrix} -j & 0 \\ 0 & 1 \end{pmatrix} e^{-j\varphi} \quad (11)$$

where φ is the phase obtained from the metasurface. Thereinto, the transmitted electric fields can be calculated as

$$\begin{pmatrix} E'_x \\ E'_y \end{pmatrix} = T \frac{1}{\sqrt{2}} \begin{pmatrix} 1 \\ 1 \end{pmatrix} e^{-jkz} e^{-j\varphi} = \frac{1}{\sqrt{2}} \begin{pmatrix} -j \\ 1 \end{pmatrix} e^{-jkz} e^{-j\varphi} \quad (12)$$

$$\vec{E}_t = (\hat{x}E'_x + \hat{y}E'_y) = \frac{1}{\sqrt{2}} (-j\hat{x} + \hat{y}) e^{-jkz} e^{-j\varphi} \quad (13)$$

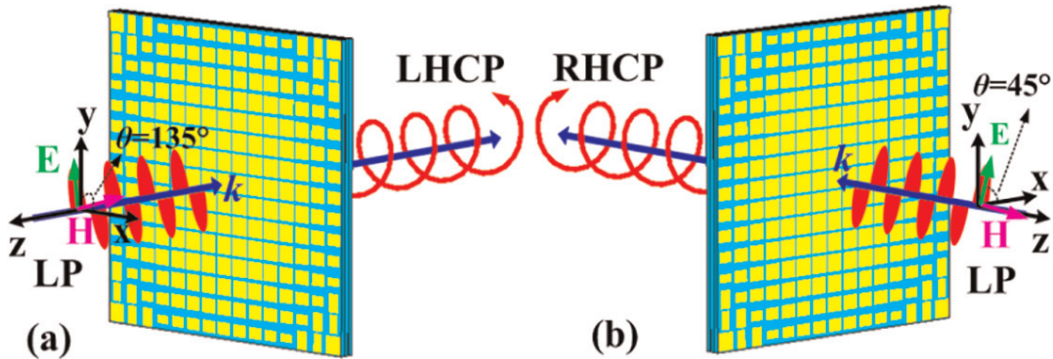


Figure 14. The proposed two schematic models of LTC polarized for different incident electric fields at (a) $\theta = 135^\circ$; (b) $\theta = 45^\circ$ relative to $+x$ direction (θ is the angle between E and $+x$ axis).

From Eq. (13), it can be concluded that a RHCP wave is obtained in this case as shown in **Figure 14b**.

In the other case of $\theta = 135^\circ$ as shown in **Figure 14a**, the transmitted electric field can be calculated as

$$\begin{pmatrix} E'_x \\ E'_y \end{pmatrix} = T \frac{1}{\sqrt{2}} \begin{pmatrix} -1 \\ 1 \end{pmatrix} e^{-jkz} e^{-j\varphi} = \frac{1}{\sqrt{2}} \begin{pmatrix} j \\ 1 \end{pmatrix} e^{-jkz} e^{-j\varphi} \quad (14)$$

$$\vec{E}_t = (\hat{x}E'_x + \hat{y}E'_y) = \frac{1}{\sqrt{2}} (j\hat{x} + \hat{y}) e^{-jkz} e^{-j\varphi} \quad (15)$$

Therefore, a LHCP wave will be obtained.

2.2 Design of the unit cell

Based on above theoretical analysis, it is necessary to design a unit cell with the ability of controlling x/y -polarized waves independently. The proposed unit cell, demonstrated in **Figure 15**, is composed of four metallic layers and three intermediate dielectric layers. Each metallic layer contains a same rectangular metal, which is employed to control the transmission phases and amplitudes of x/y -polarized EM waves. The dielectric layer has a substrate with the permittivity of $\epsilon_r = 4.3$, loss tangent of 0.001, and thickness of $h = 1$ mm. The detailed parameters are denoted by $h = 1$ mm, $p = 4.1$ mm (periodicity of the unit cell), and a_y/a_x (1–3.8 mm).

To verify the polarization-independent property for x/y -polarized EM waves, the unit cell is illuminated by a plane wave propagating along $-z$ direction as shown in **Figure 15b**. Open boundary conditions and unit cell boundary conditions are applied in the z direction and x/y direction, respectively.

To demonstrate the ability of independently manipulating different polarized waves, the 2D map of phase shifts and amplitudes versus a_x and a_y is depicted in **Figures 16** and **17**. The phases and amplitudes of T_{xx} is plotted in **Figure 16**. As a_x and a_y vary from 1 to 3.8 mm, the phase of T_{xx} shown as **Figure 16a** nearly keeps a constant, indicating that the parameter a_y has no influence on the phase of T_{xx} , while the parameter a_x has an obvious influence on the phase of T_{xx} . As shown in **Figure 16b**, varying the parameter a_y , the amplitude of T_{xx} keeps a constant, indicating that a_y has no influence on the amplitude of T_{xx} . Therefore, it is can be drawn that T_{xx} can be controlled by varying the parameter a_x independently.

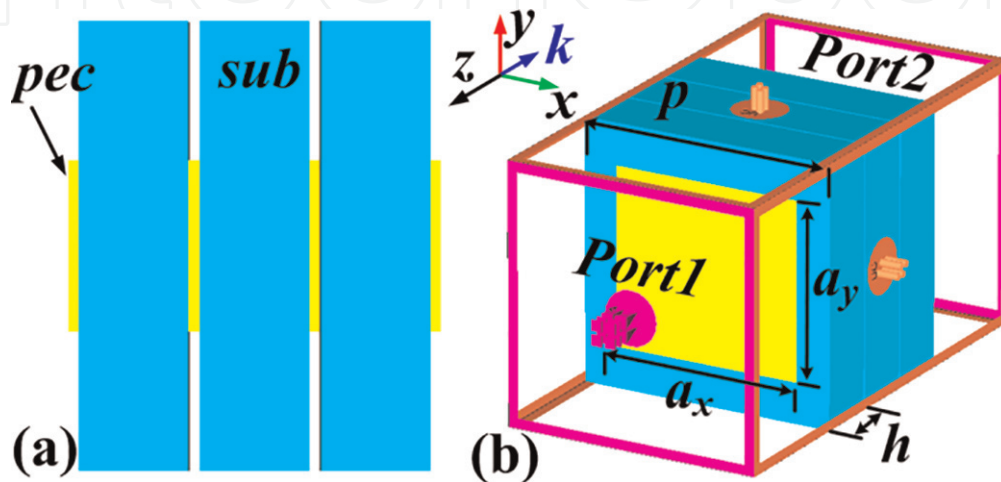


Figure 15. Structure of the unit cell and simulated setup (a) top view and (b) perspective view.

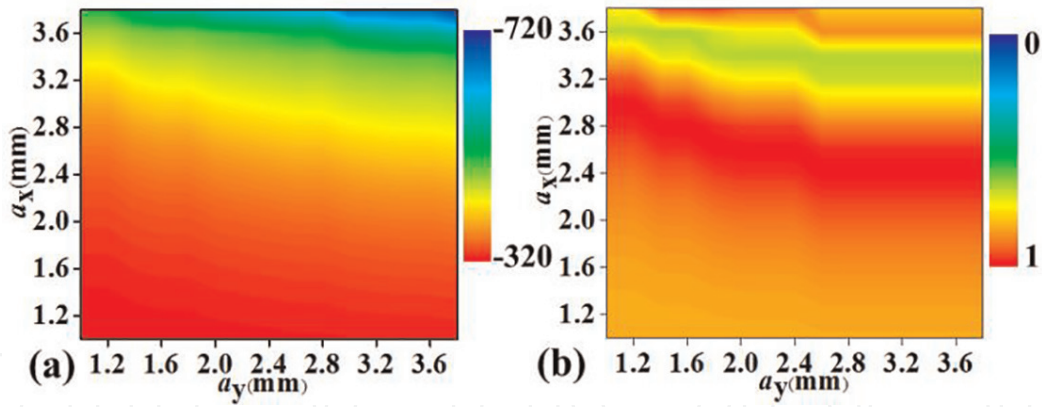


Figure 16.
 Phases and amplitudes of T_{xx} of the unit cell.

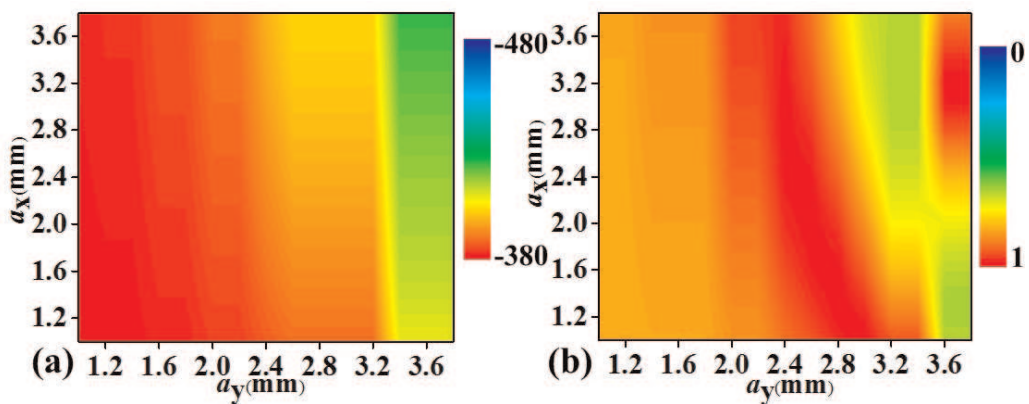


Figure 17.
 Phases and amplitudes of T_{yy} of the unit cell.

Moreover, **Figure 17** shows the phase and amplitude of T_{yy} when the unit cell is illuminated by y -polarized wave when varying a_x and a_y from 1 to 3.8 mm. As a_x and a_y vary from 1 to 3.8 mm, the phase of T_{yy} shown as **Figure 17a** nearly keeps a constant, indicating that the parameter a_x has no influence on the phase of T_{yy} , while the parameter a_y has an obvious influence on the phase of T_{yy} . As shown in **Figure 17b**, varying the parameter a_x , the amplitude of T_{yy} keeps a constant, indicating that a_x has no influence on the amplitude of T_{yy} . Therefore, it can be drawn that T_{yy} can be controlled by varying the parameter a_y independently.

Based on above analysis, it is concluded that the proposed unit cell has the ability of controlling x/y -polarized wave independently.

As we all know, the refracted wave will always deflect to the phase delay direction according to the general refraction law [3] as described in Eq. (16):

$$n_t \sin(\theta_t) - n_i \sin(\theta_i) = \frac{\lambda}{2\pi} \frac{d\varphi}{dx} \quad (16)$$

where φ is the phase discontinuity as the local position on the metasurface, $\theta_t(\theta_i)$ is the refracted (incident) angle of the EM waves, $n_t(n_i)$ is the refractive index of the transmissive (incident) medium, and λ is the wavelength. To simplify the analysis, $d\varphi/dx$ can be denoted as $2\pi/np$, where n is the number of the unit cell arranged along x direction and p is the periodicity of the unit cell. In the design, the unit cell is normally illuminated by EM wave in the free space; thus θ_i and n_t are denoted by 0° and 1, respectively. Thus the refraction angle θ_t can be depicted in Eq. (17):

$$\theta_t = \sin^{-1}\left(\frac{\lambda}{2\pi} \times \frac{2\pi}{np}\right) \quad (17)$$

To verify the performance of manipulating the x/y -polarized wave independently, one-dimensional metasurface with inverse linear phase gradient along x direction for x/y -polarized wave has been proposed in **Figure 17**. The proposed supercell is composed of six unit cells with the parameters demonstrated in **Table 1**. Phase gradients are assigned to $+60^\circ$ to -60° for x/y -polarized incident plane wave, respectively. Φ_x and Φ_y in **Table 1** represent the phase response for x/y -polarized incident waves.

4×16 supercells are fixed as **Figure 18a** has shown. The supercell is perpendicularly illuminated by plane wave along z direction in CST Microwave Studio. And open (add space) boundary condition is set along all directions.

Based on Eq. (17), the refracted angles for x/y -polarized incident wave can be calculated as 54.4° . And the refracted wave will deflect to $-x/+x$ direction, respectively. The 3D farfields are calculated as shown in **Figure 18a**. Beam 2 and beam 1 are calculated under x/y -polarized plane wave illumination, respectively. To clearly show the refracted angles for x/y -polarized waves, the normalized farfield patterns in polar are depicted in **Figure 18b**. The simulated refracted angles are in good accordance with theoretic ones calculated by Eq. (17). Therefore, a conclusion can be drawn that the phases of x/y -polarized incident waves can be manipulated by ax and ay , respectively.

2.3 Design of multifunctional transmission PGMS

Based on above unique property, it is easy to design a hyperbolic phase distribution on the multifunctional metasurface, which has the ability of polarization conversion and gain enhancement.

Index n	1	2	3	4	5	6
a_x (mm)	3.8	3.75	3.64	3.52	3.1	2.53
a_y (mm)	2.53	3.1	3.52	3.64	3.75	3.8
Φ_x (deg)	-704.3	-644.3	-584.3	-524.3	-464.3	-404.3
Φ_y (deg)	-404.3	-464.3	-524.3	-584.3	-644.3	-704.3

Table 1.
The sizes and absolute phase shifts of the six distributed unit cells.

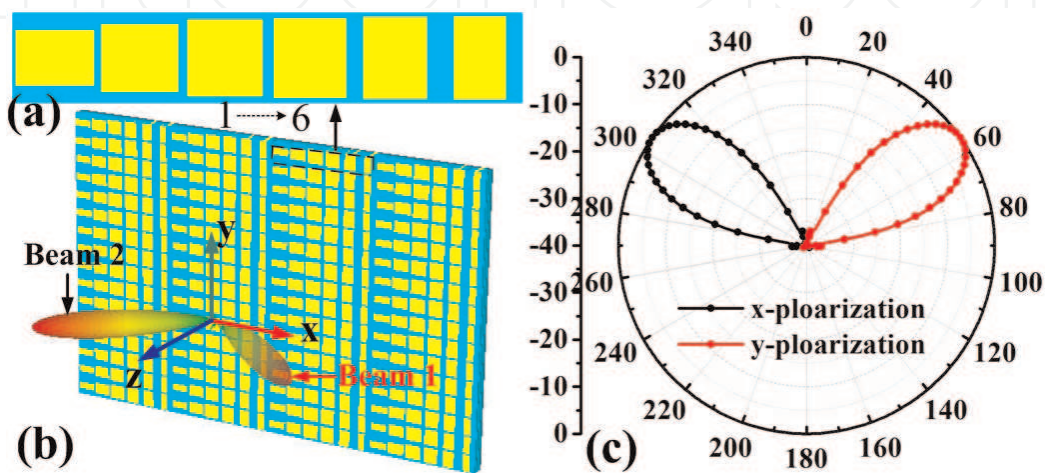


Figure 18.
(a) The supercells; (b) the designed one-dimensional phase gradient metasurface; and (c) the farfield results.

In order to efficiently convert the incident plane wave into a quasi-spherical wave, the phase $\varphi(m, n)$ at unit cell location (m, n) should be carefully optimized, yielding the following phase distribution:

$$\varphi(m, n) = \frac{2\pi}{\lambda} \left(\sqrt{(mp)^2 + (np)^2 + L^2} - L \right) + \varphi(0, 0) \quad (18)$$

where p is periodicity of unit cell and L is the focal length and m and n are the unit cell positions along x and y directions, respectively. Moreover, $\varphi(0, 0)$ represents the phase at the origin unit cell ($m = 0, n = 0$). It is easy to convert the incident plane wave into quasi-spherical wave using the above metasurface. Moreover, we concentrate on designing a linear-to-circular polarization conversion metasurface according to the theory and unique feature described in the preceding section.

In order to realize the LTC conversion, the transmitted phase for x -polarized incident wave should have a phase difference of 90° with the y -polarized incident wave through each unit cell. In this chapter, we design a LTC conversion metasurface according to **Figure 14b**. Namely, $\text{Arg}(T_{xx})_{mn} - \text{Arg}(T_{yy})_{mn} \approx -90^\circ$ should be satisfied, and a RHCP wave can be obtained. For x -polarized incident wave, the phase distribution can be denoted as

$$\text{Arg}(T_{xx})_{mn} - \text{Arg}(T_{xx})_{00} = \frac{2\pi}{\lambda} \left(\sqrt{((mp)^2 + (np)^2 + L^2)} - L \right) \quad (19)$$

For y -polarized incident wave, the phase distribution can be denoted as

$$\text{Arg}(T_{yy})_{mn} - \text{Arg}(T_{yy})_{00} = \frac{2\pi}{\lambda} \left(\sqrt{((mp)^2 + (np)^2 + L^2)} - L \right) \quad (20)$$

To achieve $\text{Arg}(T_{xx})_{mn} - \text{Arg}(T_{yy})_{mn} \approx -90^\circ$ simply, the phase difference $\text{Arg}(T_{xx})_{00} - \text{Arg}(T_{yy})_{00} \approx -90^\circ$ should be satisfied for x/y -polarized incident waves at origin point $\varphi(0, 0)$.

Based on above analysis, the multifunctional transmission metasurface is composed of 15×15 unit cells. The working frequency and focal length are $f = 15$ GHz and $L = 30$ mm, respectively. A patch antenna, operating from 14.5 to 15.3 GHz, is placed on the focal point to be a feed source. By insertion of $p = 4.1$ mm, $\lambda = 20$ mm,

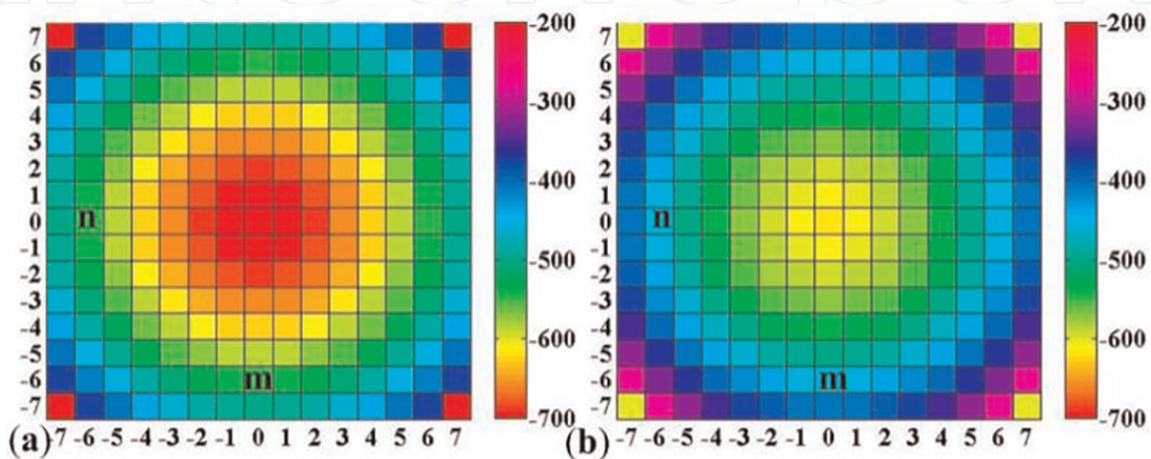


Figure 19.
 Absolute phase distributions for (a) x polarization and (b) y polarization.

$L = 30$ mm, and $\text{Arg}(T_{xx})_{00} = -704.3^\circ$ into Eqs. (19) and (20), the phase distribution for the x/y polarization waves is calculated as **Figure 19**. Finally, the proposed multifunctional transmission metasurface is depicted in **Figure 20a**.

To verify the proposed multifunctional transmission metasurface's function of focusing EM wave at $L = 30$ mm, the metasurface is simulated in CST. As shown in **Figure 20a**, the metasurface is normally illuminated by a plane wave with $\theta = 45^\circ$ along the x axis, and a curve is put along z axis to evaluate power field on curve to calculate the focal point. Besides, a power flow monitor is set at 15 GHz. It is obvious that the plane wave is focused to a pink focal spot and the maximum power field is at $L = 30$ mm.

2.4 High-gain lens antenna design

A designed patch antenna, operating at 15 GHz, is put at the focal point of the multifunctional metasurface. As **Figure 20** has shown, the polarization of EM wave emitted by the feed source antenna has an angle of $\theta = 45^\circ$ along the x axis. To clearly show the function of proposed lens antenna, simulated 3D radiation pattern at 15 GHz and measured S_{11} of the lens antenna are plotted in **Figure 21**. It is

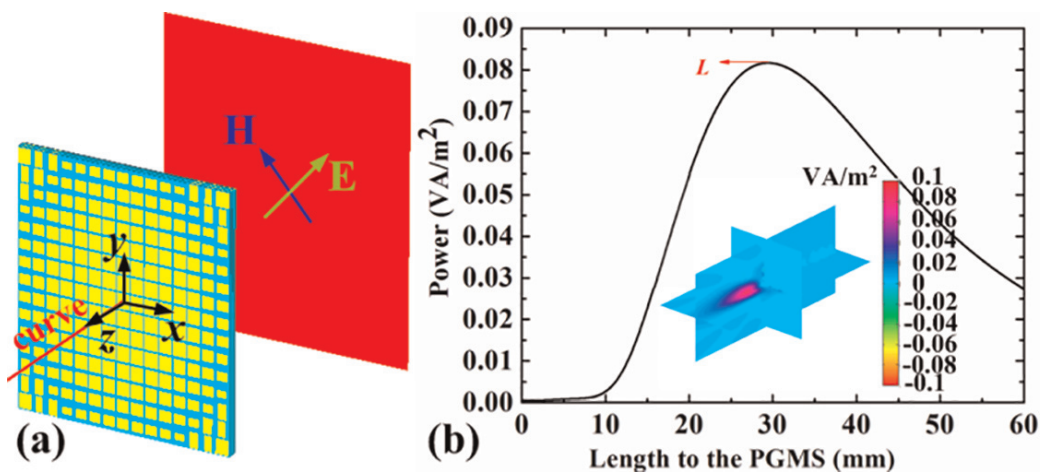


Figure 20.

(a) The multifunctional transmission PGMS and simulated conditions and (b) power field distribution in xoz and yoz planes and power field distribution along z axis.

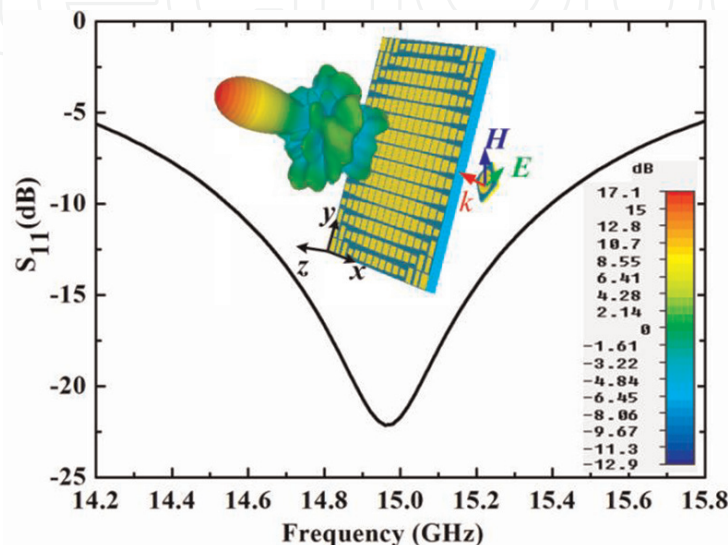


Figure 21.

The simulated 3D radiation pattern and measured S_{11} of lens antenna.

obvious that the pencil-beam 3D radiation pattern is obtained and realized gain has been enhanced remarkably.

Furthermore, the near-field electric field distributions in xoz and yoz planes have been depicted in **Figure 22**. The incident wave has been converted into near-plane wave through the proposed metasurface. The simulated result is in line with our expectation.

Lastly, a sample is fabricated and measured in a microwave anechoic chamber as shown in **Figure 23**. And simulated and measured 2D radiation patterns of lens antenna are plotted in **Figure 24**. As shown in **Figure 24**, the co-polarization and cross-polarization of simulation and measurement are plotted in two orthogonal planes. And the simulated results are in good accordance with the measured ones. Compared with patch antenna, the radiation patterns of proposed multifunctional antenna are more directional. The measured peak gain of patch antenna and proposed multifunctional antenna is about 5.9 and 16.9 dB at 15 GHz, respectively. And the realized gain has been enhanced with 11 dB at 15 GHz, and calculated aperture efficiency is about 41.2%. Comparing co-polarization with cross-polarization at $\theta = 0^\circ$, we find that the isolation is better than 17 dB.

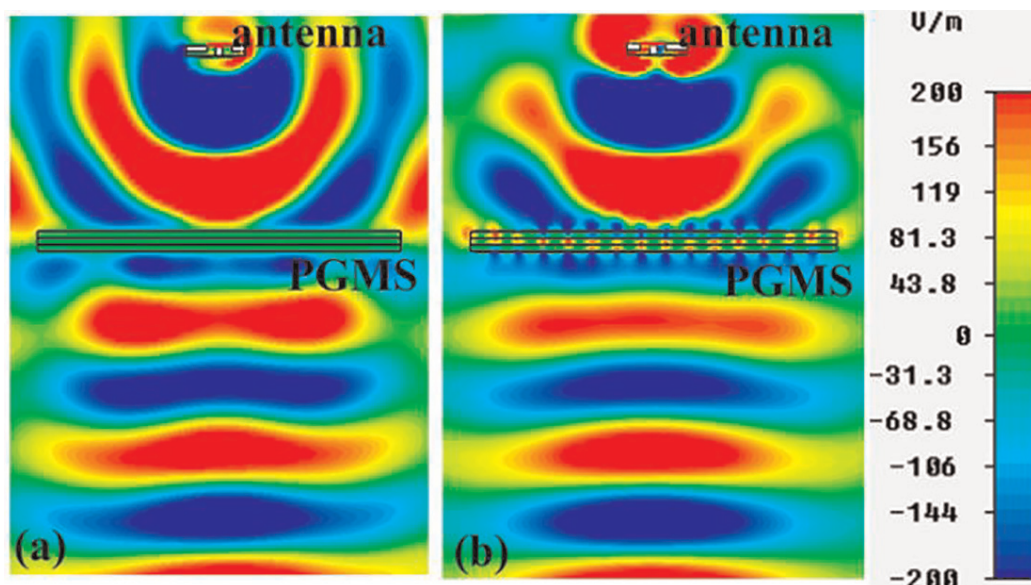


Figure 22.
Electric field distributions in (a) xoz and (b) yoz plane at 15 GHz.

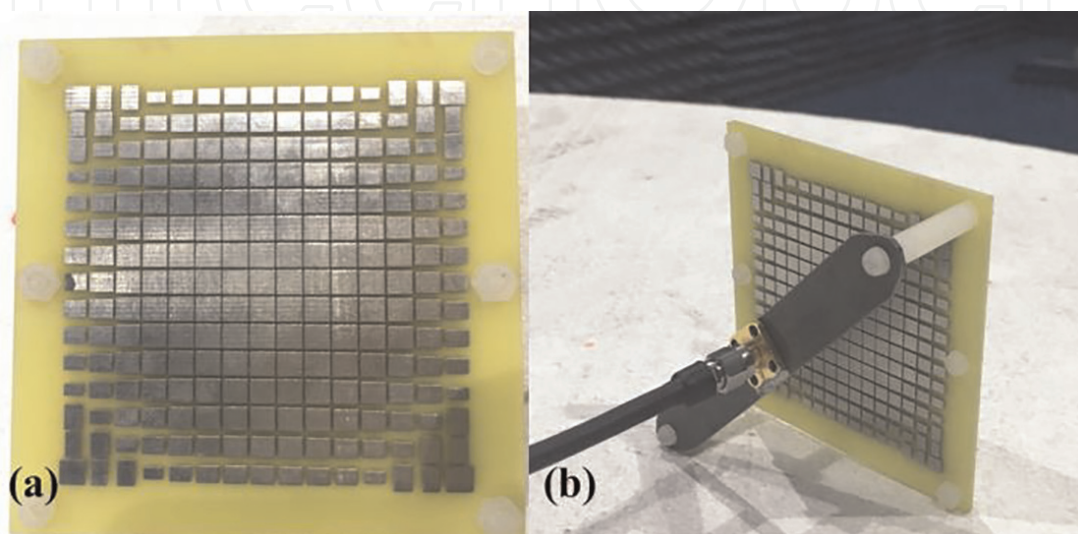


Figure 23.
The photographs of (a) PGMS top view and (b) lens antenna.

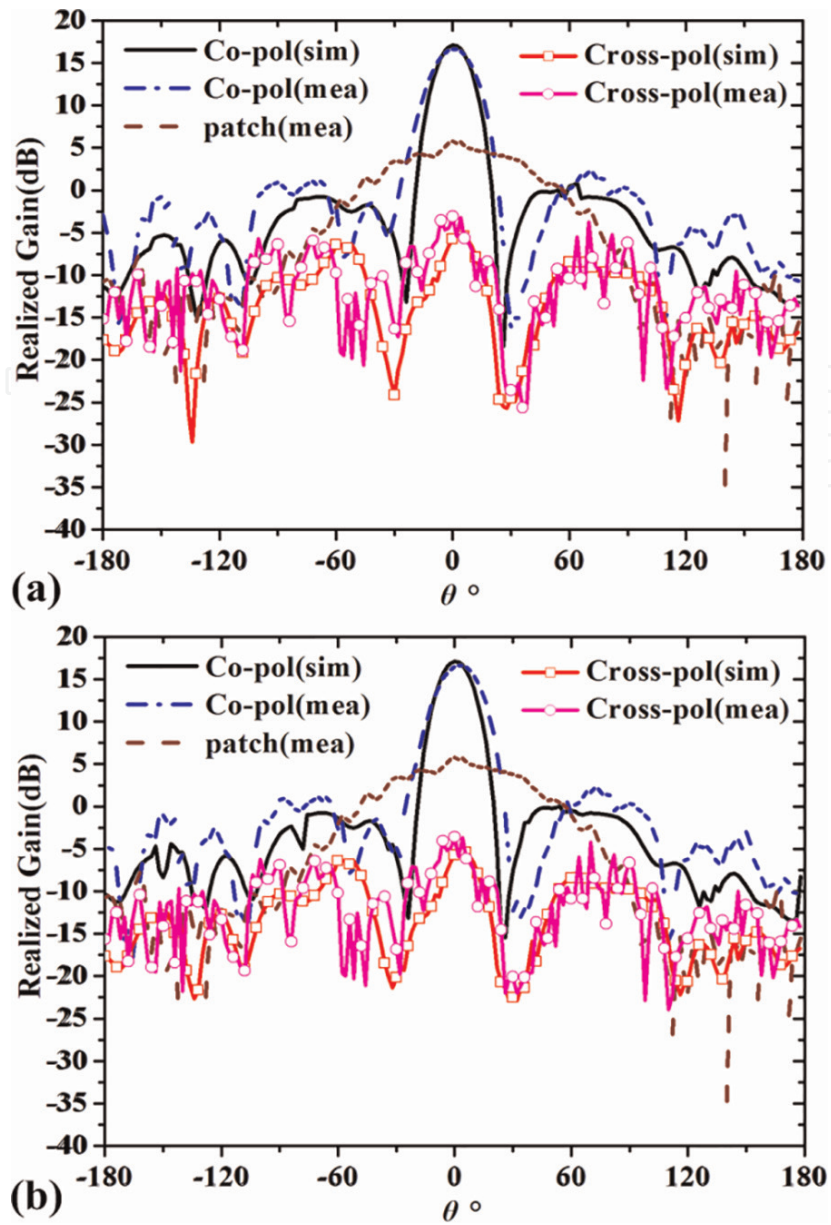


Figure 24. 2D radiation patterns at 15 GHz. (a) xoy plane and (b) yoz plane.

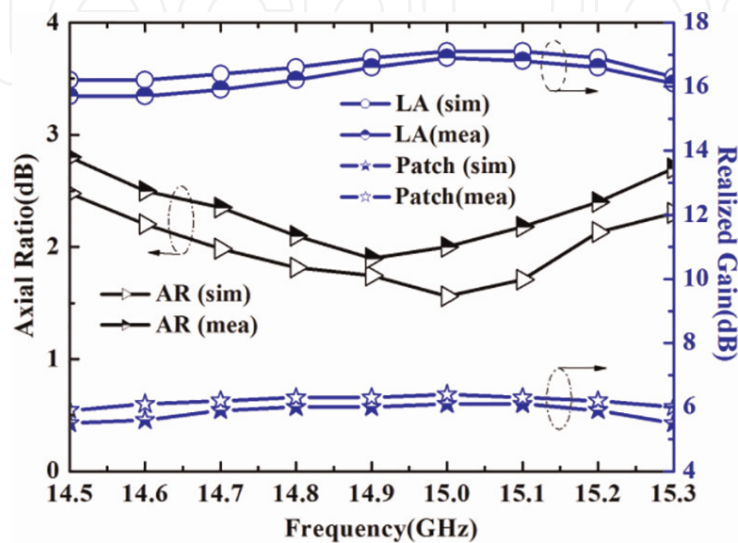


Figure 25. Simulated and measured realized gain for patch antenna and lens antenna and axial ratio.

Moreover, the simulated and measured axial ratios (AR) ($\theta = 0^\circ$) are plotted in **Figure 25**. The simulated and measured realized gain of lens antenna and patch antenna is described in **Figure 25**. All the simulated and measured results are in good accordance. It is obvious that the gain enhancement is about 11 dB at 15 GHz. Besides, the axial ratio bandwidth for $AR < 3$ dB ranges from 14.5 to 15.3 GHz with the fractional bandwidth 5.3%. And we find that the 1-dB gain bandwidth is 5.3% (14.5–15.3 GHz), which agrees well with the axial ratio bandwidth.

Conclusions

In this chapter, we have reviewed our recent efforts in utilizing metasurface to enhance the performance of the conventional antenna. For the reflected metasurface, we propose a new broadband, single-layered reflected focusing metasurface, and take it into application for high-gain planar antenna. The metasurface exhibits good focusing phenomenon from 15 to 22 GHz. Both simulation and measured results show that the peak gain of planar antenna has been averagely enhanced by 16 and -1 dB gain bandwidth which is from 15 to 22 GHz, while for the transmitted metasurface, a novel multifunctional metasurface combining linear-to-circular polarization conversion and EM waves focusing has been proposed and applied to designed a high-gain lens antenna. A RHCP lens antenna is simulated and measured. The measured results show that the lens antenna can convert LP waves into RHCP waves at 15 GHz. The 3-dB axial ratio bandwidth is 5.3%. Realized gain at 15 GHz is 16.9 dB, corresponding to aperture efficiency of 41.2%. These above metasurface antennas not only open up a new route for the applications of focusing metasurfaces in microwave band but also afford an alternative for high-performance antennas.

Acknowledgements


The authors would like to express their gratitude to anonymous reviewers for their helpful comments and China North Electronic Engineering Research Institute for the fabrication. This work was supported by the National Natural Science Foundation of China (Grant Nos. 61372034).

Author details

Haisheng Hou, Haipeng Li*, Guangming Wang*, Tong Cai, Xiangjun Gao and Wenlong Guo
Microwave Laboratory, Air Force Engineering University, Xi'an, China

*Address all correspondence to: s_lihaipeng@sina.cn and wgming01@sina.com

IntechOpen

© 2019 The Author(s). Licensee IntechOpen. This chapter is distributed under the terms of the Creative Commons Attribution License (<http://creativecommons.org/licenses/by/3.0>), which permits unrestricted use, distribution, and reproduction in any medium, provided the original work is properly cited. 

References

- [1] Li HP, Wang GM, Gao XJ, Liang JG, Hou HS. Novel metasurface for dual-mode and dual flat high-gain antenna application. *IEEE Transactions on Antennas and Propagation*. 2018;**66**(7): 3706-3711
- [2] Li HP, Wang GM, Cai T, Liang JG, Gao XJ. Phase- and amplitude-control metasurfaces for antenna main-lobe and sidelobe manipulations. *IEEE Transactions on Antennas and Propagation*. 2018;**66**(10):5121-5129
- [3] Biswas SR, Gutierrez CE, Nemilentsau A, Lee IH, Oh SH, Avouris P, et al. Tunable graphene metasurface reflectarray for cloaking, illusion, and focusing. *Physical Review Applied*. 2018;**9**(3):034021
- [4] Liang JJ, Huang GL, Zhao JN, Gao ZJ, Yuan T. Wideband phase-gradient metasurface antenna with focused beams. *IEEE Access*. 2019;**7**:20767-20772
- [5] Katore KK, Chandravanshi S, Biswas A, Akhtar MJ. Realization of split beam antenna using transmission-type coding metasurface and planar lens. *IEEE Transactions on Antennas and Propagation*. 2019;**67**(4):2074-2084
- [6] Yang WC, Gu LZ, Che WQ, Meng Q, Xue Q, Wan C. A novel steerable dual-beam metasurface antenna based on controllable feeding mechanism. *IEEE Transactions on Antennas and Propagation*. 2019;**67**(2): 784-793
- [7] Yu NF, Genevet P, Kats MA, Aieta F, Tetienne J-P, Capasso F, et al. Light propagation with phase discontinuities: Generalized laws of reflection and refraction. *Science*. 2011;**334**:333-337
- [8] Wong AMH, Eleftheriades GV. Perfect anomalous reflection with a bipartite Huygens' metasurface. *Physical Review X*. 2018;**8**(1):011036
- [9] Xu WK, Zhang M, Ning JY, Wang W, Yang TZ. Anomalous refraction control of mode-converted elastic wave using compact notch-structured metasurface. *Material Research Express*. 2019;**6**(6): 065802
- [10] Asadpor L, Sharifi G, Rezvani M. Design of a high-gain wideband antenna using double-layer metasurface. *Microwave and Optical Technology Letters*. 2019;**61**(4):1001-1010
- [11] Ling YH, Huang LR, Hong W, Liu TJ, Jing L, Liu WB, et al. Polarization-switchable and wavelength-controllable multi-functional metasurface for focusing and surface-plasmon-polariton wave excitation. *Optics Express*. 2017;**25**(24): 29812-29821
- [12] Meng YY, Ma H, Li YF, Feng MD, Wang JF, Li ZQ, et al. Spoof surface plasmon polaritons excitation and wavefront control by Pancharatnam-Berry phase manipulating metasurface. *Journal of Physics D: Applied Physics*. 2018;**51**(21):215302
- [13] Lin BQ, Guo JX, Chu P, Huo WJ, Xing Z, Huang BG, et al. Multiple-band linear-polarization conversion and circular polarization in reflection mode using a symmetric anisotropic metasurface. *Physical Review Applied*. 2018;**9**:024038
- [14] Jia YT, Liu Y, Zhang WB, Wang J, Wang YZ, Gong SX, et al. Ultra-wideband metasurface with linear-to-circular polarization conversion of an electromagnetic wave. *Optical Materials Express*. 2018;**8**(3):597-604
- [15] Zheng Q, Guo CJ, Ding J. Wideband metasurface-based reflective polarization converter for linear-to-linear and linear-to-circular polarization conversion. *IEEE Antennas and*

Wireless Propagation Letters. 2018;
17(8):1459-1463

[16] Khan MI, Khalid Z, Tahir FA. Linear and circular-polarization conversion in X-band using anisotropic metasurface. Scientific Reports. 2019;**9**:4552

[17] Ratni B, de Lustrac A, Plau GP, Burokur SN. Electronic control of linear-to-circular polarization conversion using a reconfigurable metasurface. Applied Physics Letters. 2017;**111**(21):214101

[18] Wang W, Guo ZY, Ran LL, Sun YX, Shen F, Li Y, et al. Polarization-independent characteristics of the metasurfaces with the symmetrical axis's orientation angle of 45° or 135°. Journal of Optics. 2016;**18**:035007

[19] Menzel C, Rockstuhl C, Lederer F. Advanced Jones calculus for the classification of periodic metamaterials. Physical Review A. 2010;**82**:053811